Theory of exciton doublet structures and polarization relaxation in single quantum dots

T. Takagahara*
NTT Basic Research Laboratories, 3-1 Morinosato Wakamiya, Atsugi-shi 243-0198, Japan
(Received 22 March 2000; revised manuscript received 25 August 2000)

The mechanism of exciton doublet structures in quantum dots is identified as the long-range part of the electron-hole exchange interaction which is emphasized by the anisotropic shape of quantum dots. The physical origin of the energetic order of the orthogonally polarized exciton states of each doublet is clarified by inspecting the spatial distribution of the exciton polarization. The key concepts to understand the energetic order are the node configuration of the distribution function of exciton polarization and the dipole-dipole interaction energy originating from the long-range electron-hole exchange interaction. The population relaxation and the polarization relaxation of excitons are studied and the extremely slow polarization relaxation within exciton doublet states is predicted. It is also found that the inter-doublet cross-relaxation between orthogonally polarized exciton states occurs as efficiently as the population relaxation.

I. INTRODUCTION

The spatial confinement of electrons and holes along all three dimensions leads to a discrete energy level structure with sharp optical absorption lines. In this sense a semiconductor quantum dot (QD) can be regarded as an artificial solid-state atom. The concentration of the oscillator strength to sharp exciton transitions makes QD's very attractive for electro-optic and nonlinear optical applications. To be more specific, QD's are considered as promising elements for implementing the coherent control of the quantum state,[1] which is an essential function to achieve quantum information processing and quantum computation.[2] The excitonic wave function has been manipulated by controlling the optical phase of the pulse sequence through timing and polarization and the wave-function engineering in semiconductor QD's is now being developed.[1] In this wave-function manipulation, important features are the sharp spectral lines indicating a long coherence time and well-defined polarization characteristics. In this paper we discuss the origin of the recently observed exciton doublet structures, their polarization characteristics and the dynamics of polarization relaxation among these exciton states.

Recently, very fine structures were observed in exciton photoluminescence (PL) from GaAs quantum wells (QW's).[3–5] These sharp lines are interpreted as luminescence from localized excitons at island structures in QW. These island structures can be regarded as zero-dimensional quantum dots (QD's). Furthermore, in the photoluminescence excitation spectra, doublet structures with mutually orthogonal linear polarizations were discovered. The direction of linear polarization is closely related to the geometrical shape of the QW islands. As observed by the scanning tunneling microscopy,[5] QW islands are elongated along the $[1\bar{1}0]$ direction. Correspondingly, the exciton states are polarized along the $[1\bar{1}0]$ or [110] direction. The splitting energy of each doublet states is about several tens of micro eV and is of the same order of magnitude as the exciton LT (longitudinal-transverse) splitting energy in bulk GaAs. From these experimental results, we can deduce that these splittings arise from the electron-hole exchange interaction, especially its long-range part which is sensitively dependent on the geometrical shape of quantum dots. Recently the important role of the electron-hole exchange interaction in the exciton fine structures has been discussed for III-V and II-VI semiconductor quantum dots.[6–9] A theory of the exciton fine structure in quantum dots was presented taking into account only the heavy-hole band.[10] But actually the heavy-hole band and the light-hole band are mixed together. In this simple theory the doublet lines have the same oscillator strength and the experimental details cannot be explained, e.g., the asymmetric shape of the excited exciton doublets.

Thus the primary purposes of this paper are to develop a microscopic theory of the electron-hole exchange interaction in semiconductor quantum dots and to clarify the exciton fine structures in detail, e.g., the relation between the energetic order of the polarized doublet states and the node configuration of the distribution function of the exciton polarization. At the same time, the exciton dynamics or the exciton dephasing is the key issue in estimating the feasibility of the quantum coherent control in general. The exciton dephasing in quantum dots was discussed by the present author[11] in conjunction with the linewidth of the very sharp PL lines. Recently Bonadeo *et al.*[12] carried out the pump-probe spectroscopy on a GaAs single quantum dot and estimated the population relaxation rates among individual exciton levels. Also Gotoh *et al.*[13] reported the exciton spin relaxation time in an InGaAs quantum dot. These dynamical studies are important to clarify the relaxation mechanisms in quantum dots and to estimate the ultimate limit of the exciton coherence time. Here we discuss in detail the population relaxation and the polarization relaxation among the exciton doublet structures and investigate the efficiency of cross-relaxation between the orthogonally polarized exciton states. A part of these results was preliminarily reported in Ref. 14.

This paper is organized as follows. In Sec. II, the electron-hole exchange interaction in quantum dots is analyzed extensively with emphasis on its long-range part and the method of calculation is presented. In Sec. III, the calculated exciton doublet structures are discussed concerning their dependence on the size, shape, and depth of the con-

 ©2000 The American Physical Society

finement potential. In Sec. IV, the physical origin of the energetic order of the orthogonally polarized exciton states of each doublet is clarified by inspecting the spatial distribution of the exciton polarization. In Sec. V, the population and the polarization relaxation processes among exciton doublet structures are discussed and it is discovered that the cross-relaxation between the orthogonally polarized exciton states occurs as efficiently as the population relaxation without the change of the polarization direction.[14] In order to see the efficient polarization relaxation more clearly, we examine in Sec. VI the photoluminescence spectra under selective excitation and the excitation spectra of photoluminescence. Finally, our results and predictions are summarized in Sec. VII.

II. ELECTRON-HOLE EXCHANGE INTERACTION IN QUANTUM DOTS

We formulate a theory of excitons in a quantum dot taking into account the multiband structure of the valence band and the electron-hole exchange interaction. For the valence band, we take into account four states belonging to the Γ_8 symmetry ($J=3/2$) and employ the full Luttinger Hamiltonian[15] without making the spherical approximation. We neglect the spin-orbit-split $J=1/2$ valence band because the splitting energy between the $J=3/2$ and the $J=1/2$ valence bands is much larger than the typical energy level spacings to be discussed in this paper. Then we denote two conduction band Bloch functions by $|c\tau\rangle$ where τ indicates the spin-up(α) or the spin-down(β) state and similarly four valence band Bloch functions by $|v\sigma\rangle$ where σ stands for the z-component of the angular momentum (3/2, 1/2, $-1/2$, $-3/2$). Thus the exciton state is composed of 8 combinations of the conduction band and the valence band, namely

$$|X\rangle=\sum_{\tau,\sigma}\sum_{r_e,r_h} f_{\tau\sigma}(r_e,r_h)a^{\dagger}_{c\tau r_e}a_{v\sigma r_h}|0\rangle, \tag{2.1}$$

where the Wannier function representation of the annihilation and creation operators is used and $f_{\tau\sigma}$ is the envelope function. The eigenvalue equation for $f_{\tau\sigma}$ is given as

$$\sum_{\tau'\sigma' r_e' r_h'} H(c\tau r_e, v\sigma r_h; c\tau' r_e', v\sigma' r_h') f_{\tau'\sigma'}(r_e', r_h') = E\ f_{\tau\sigma}(r_e, r_h) \tag{2.2}$$

with

$$\begin{aligned} H(c\tau r_e, v\sigma r_h; c\tau' r_e', v\sigma' r_h') &= \delta_{\sigma\sigma'}\delta_{r_h r_h'}(\epsilon_{c\tau,c\tau'}(-i\nabla_e)+\delta_{\tau\tau'}v_e(r_e)) \\ &\quad -\delta_{\tau\tau'}\delta_{r_e r_e'}(\epsilon_{v\sigma',v\sigma}(i\nabla_h)+\delta_{\sigma\sigma'}v_h(r_h)) \\ &\quad +V(c\tau r_e, v\sigma' r_h'; c\tau' r_e', v\sigma r_h) \\ &\quad -V(c\tau r_e, v\sigma' r_h'; v\sigma r_h, c\tau' r_e'), \end{aligned} \tag{2.3}$$

where $\epsilon_{c\tau,c\tau'}(\epsilon_{v\sigma',v\sigma})$ is the band energy of the conduction (valence) band electron, $v_e(v_h)$ is the confinement potential for the conduction (valence) band electron and $V(i,j;k,l)$ is the Coulomb or exchange matrix element defined by

$$V(i,j;k,l)=\int d^3r \int d^3r'\ \ \phi_i^*(r)\phi_j^*(r') \times\frac{e^2}{\epsilon|r-r'|}\phi_k(r')\phi_l(r) \tag{2.4}$$

in terms of the Wannier functions $\{\phi_i\}$ and the dielectric constant ϵ. $\epsilon_{c\tau,c\tau'}$ is simply approximated as

$$\epsilon_{c\tau,c\tau'}(k)=-\frac{\hbar^2}{2m_e}k^2\delta_{\tau\tau'} \tag{2.5}$$

with the effective mass m_e and $\epsilon_{v\sigma',v\sigma}(k)$ is the Luttinger Hamiltonian given by

$$\begin{aligned} -\frac{\hbar^2}{m_0}\Big[&\left(\gamma_1+\frac{5}{2}\gamma_2\right)\frac{k^2}{2}-\gamma_2(k_x^2J_x^2+k_y^2J_y^2+k_z^2J_z^2) \\ &-\gamma_3k_yk_z(J_yJ_z+J_zJ_y)-\gamma_3k_zk_x(J_zJ_x+J_xJ_z) \\ &-\gamma_3k_xk_y(J_xJ_y+J_yJ_x)\Big] \end{aligned} \tag{2.6}$$

in terms of the Luttinger parameters γ_1, γ_2 and γ_3, the free electron mass m_0 and the angular momentum operators J_x, J_y, and J_z for $J=3/2$. Recently, the significance of the operator ordering in the Luttinger Hamiltonian was pointed out in conjunction with the interface-induced effects.[16] The exciton energy level structure on the order of a few meV may be affected by the operator ordering but be influenced more importantly by the actual morphology of the islandlike quantum dot in a quantum well. However, the main issue of this paper is the doublet splitting of each exciton level due to the electron-hole exchange interaction which is of the order of tens of micro eV and is much smaller than the exciton level spacing. Thus the operator ordering in the Luttinger Hamiltonian is not relevant and will not be taken into account in this paper. The Coulomb matrix element can be approximated due to the localized nature of the Wannier functions as

$$V(c\tau r_e, v\sigma' r_h'; v\sigma r_h, c\tau' r_e') \approx \delta_{r_e r_e'}\delta_{r_h r_h'}\delta_{\tau\tau'}\delta_{\sigma\sigma'}\frac{e^2}{\epsilon|r_e-r_h|}. \tag{2.7}$$

The exchange term can also be approximated as

$$\begin{aligned} V(c\tau r_e, v\sigma' r_h'; c\tau' r_e', v\sigma r_h) &\approx \delta_{r_e r_h}\delta_{r_e' r_h'}[\delta_{r_e r_e'}V(c\tau r_e, v\sigma' r_e; c\tau' r_e, v\sigma r_e) \\ &\quad +(1-\delta_{r_e r_e'})V(c\tau r_e, v\sigma' r_e'; c\tau' r_e', v\sigma r_e)]. \end{aligned} \tag{2.8}$$

The first (second) term in the parentheses is usually called the short-range (long-range) exchange term. The long-range term can be decomposed into the multipole expansion and the lowest-order term is retained as

$$V(c\tau r_e, v\sigma' r_e'; c\tau' r_e', v\sigma r_e) \approx \vec{\mu}_{c\tau,v\sigma} \frac{[1-3\vec{n}\cdot{}^t\vec{n}]}{|r_e - r_e'|^3} \vec{\mu}_{v\sigma',c\tau'} \tag{2.9}$$

with

$$\vec{n} = \frac{\vec{r_e} - \vec{r_e'}}{|r_e - r_e'|}, \tag{2.10}$$

$$\vec{\mu}_{c\tau,v\sigma} = \int d^3r \;\; \phi^*_{c\tau R}(r)(\vec{r} - \vec{R})\phi_{v\sigma R}(r), \tag{2.11}$$

where $\phi_{c\tau(v\sigma)R}(r)$ is a Wannier function localized at the site R. Hereafter the vector symbols will be dropped because of no fear of confusion. Thus the long-range exchange term is described as the dipole-dipole interaction between the exciton transition dipole moments. In the calculation of the matrix elements of this long-range exchange term, the singular nature in Eq. (2.9) can be avoided by a mathematical artifice.[17,11] As a result, we have

$$\begin{aligned}
&\sum_{r_e \neq r_e'} f^*_{\tau\sigma}(r_e, r_e) f_{\tau'\sigma'}(r_e', r_e') \mu_{c\tau,v\sigma} \frac{[1-3n\cdot{}^t n]}{|r_e - r_e'|^3} \mu_{v\sigma',c\tau'} \\
&\quad = -\frac{4\pi}{3}(\mu_{c\tau,v\sigma} \cdot \mu_{v\sigma',c\tau'}) \\
&\qquad \times \int d^3r \;\; f^*_{\tau\sigma}(r,r) f_{\tau'\sigma'}(r,r) \\
&\qquad + \int d^3r \;\; \mathrm{div}_r (f^*_{\tau\sigma}(r,r)\mu_{c\tau,v\sigma}) \\
&\qquad \times \mathrm{div}_r \left[\int d^3r' \;\; \frac{\mu_{v\sigma',c\tau'}}{|r - r'|} f_{\tau'\sigma'}(r', r') \right].
\end{aligned} \tag{2.12}$$

It can be shown that this long-range exchange term vanishes for the s-like envelope functions.[17] Thus the admixture of the higher angular-momentum states is necessary to have a finite magnitude of the long-range exchange energy, which would be induced by the anisotropic shape of quantum dots or by the strained environment around the quantum dots.[18] On the other hand, the matrix element of the short-range exchange term is simply given as

$$V(c\tau r_0, v\sigma' r_0; c\tau' r_0, v\sigma r_0) \int d^3r \;\; f^*_{\tau\sigma}(r,r) f_{\tau'\sigma'}(r,r). \tag{2.13}$$

Now we proceed to a more detailed calculation of these matrix elements. The angular momentum and spin parts of the $J = 3/2$ valence-band Bloch functions can be written as

$$\begin{aligned}
\left| \frac{3}{2} \frac{3}{2} \right\rangle &= |v_1\rangle = Y_{11}\alpha, \\
\left| \frac{3}{2} \frac{1}{2} \right\rangle &= |v_2\rangle = \sqrt{\frac{2}{3}} Y_{10}\alpha + \sqrt{\frac{1}{3}} Y_{11}\beta, \\
\left| \frac{3}{2} -\frac{1}{2} \right\rangle &= |v_3\rangle = \sqrt{\frac{1}{3}} Y_{1-1}\alpha + \sqrt{\frac{2}{3}} Y_{10}\beta, \\
\left| \frac{3}{2} -\frac{3}{2} \right\rangle &= |v_4\rangle = Y_{1-1}\beta,
\end{aligned} \tag{2.14}$$

where $\alpha(\beta)$ denotes the up(down) spin state. Then we can identify the nonzero matrix elements of the short-range exchange interaction at the same site r_0 as

$$\begin{aligned}
V(c\alpha r_0, v_1 r_0; c\alpha r_0, v_1 r_0) &= V(c\beta r_0, v_4 r_0; c\beta r_0, v_4 r_0) \\
&= E_X^S, \\
V(c\alpha r_0, v_2 r_0; c\alpha r_0, v_2 r_0) &= V(c\beta r_0, v_3 r_0; c\beta r_0, v_3 r_0) \\
&= \frac{2}{3} E_X^S, \\
V(c\alpha r_0, v_3 r_0; c\alpha r_0, v_3 r_0) &= V(c\beta r_0, v_2 r_0; c\beta r_0, v_2 r_0) \\
&= \frac{1}{3} E_X^S, \\
V(c\alpha r_0, v_2 r_0; c\beta r_0, v_1 r_0) &= V(c\beta r_0, v_1 r_0; c\alpha r_0, v_2 r_0) \\
&= \sqrt{\frac{1}{3}} E_X^S, \\
V(c\alpha r_0, v_3 r_0; c\beta r_0, v_2 r_0) &= V(c\beta r_0, v_2 r_0; c\alpha r_0, v_3 r_0) \\
&= \frac{2}{3} E_X^S, \\
V(c\alpha r_0, v_4 r_0; c\beta r_0, v_3 r_0) &= V(c\beta r_0, v_3 r_0; c\alpha r_0, v_4 r_0) \\
&= \sqrt{\frac{1}{3}} E_X^S,
\end{aligned} \tag{2.15}$$

with

$$\begin{aligned}
E_X^S = \frac{4\pi e^2}{3} \int dr \;\; r^2 \int dr' \;\; (r')^2 \;\; \phi_s(r)\phi_p(r') \\
\times \frac{r_<}{r_>^2} \phi_s(r')\phi_p(r),
\end{aligned} \tag{2.16}$$

where $r_< = \min(r, r')$, $r_> = \max(r, r')$ and $\phi_s(\phi_p)$ denotes the radial part of the $s(p)$-like Wannier function at a site.

As mentioned before, the exciton is a linear combination state with respect to the electron-hole pair index $\tau\sigma$ in Eq. (2.1), namely $\alpha v_1, \alpha v_2, \alpha v_3, \alpha v_4, \beta v_1, \beta v_2, \beta v_3$, and βv_4 [$v_1 \sim v_4$ are defined in Eq. (2.14)]. The short-range exchange term in this 8×8 matrix representation is given as

$$H_{exch}^{SR}=\begin{pmatrix} |\alpha v_1\rangle & |\alpha v_2\rangle & |\alpha v_3\rangle & |\alpha v_4\rangle & |\beta v_1\rangle & |\beta v_2\rangle & |\beta v_3\rangle & |\beta v_4\rangle \\ 1 & 0 & 0 & 0 & 0 & \sqrt{\frac{1}{3}} & 0 & 0 \\ 0 & \frac{2}{3} & 0 & 0 & 0 & 0 & \frac{2}{3} & 0 \\ 0 & 0 & \frac{1}{3} & 0 & 0 & 0 & 0 & \sqrt{\frac{1}{3}} \\ 0 & 0 & 0 & 0 & 0 & 0 & 0 & 0 \\ 0 & 0 & 0 & 0 & 0 & 0 & 0 & 0 \\ \sqrt{\frac{1}{3}} & 0 & 0 & 0 & 0 & \frac{1}{3} & 0 & 0 \\ 0 & \frac{2}{3} & 0 & 0 & 0 & 0 & \frac{2}{3} & 0 \\ 0 & 0 & \sqrt{\frac{1}{3}} & 0 & 0 & 0 & 0 & 1 \end{pmatrix}\cdot E_X^S\ , \tag{2.17}$$

where the first line in the matrix is inserted to indicate the Bloch function bases and each matrix element is a block matrix having the dimension of the number of the envelope function bases.

The matrix elements of the interband transition in Eq. (2.11) which appear in the long-range exchange term are given as

$$\langle c\alpha|\vec{r}|v_1\rangle=(-1,-i,0)\mu,\quad \langle c\alpha|\vec{r}|v_2\rangle=\left(0,0,\frac{2}{\sqrt{3}}\right)\mu,$$

$$\langle c\alpha|\vec{r}|v_3\rangle=\left(\frac{1}{\sqrt{3}},\frac{-i}{\sqrt{3}},0\right)\mu,\quad \langle c\alpha|\vec{r}|v_4\rangle=(0,0,0),$$

$$\langle c\beta|\vec{r}|v_1\rangle=(0,0,0),\quad \langle c\beta|\vec{r}|v_2\rangle=\left(\frac{-1}{\sqrt{3}},\frac{-i}{\sqrt{3}},0\right)\mu,$$

$$\langle c\beta|\vec{r}|v_3\rangle=\left(0,0,\frac{2}{\sqrt{3}}\right)\mu,\quad \langle c\beta|\vec{r}|v_4\rangle=(1,-i,0)\mu \tag{2.18}$$

with

$$\mu=\sqrt{\frac{2\pi}{3}}\int_0^\infty dr\ \ r^2\phi_s(r)\ \ r\ \ \phi_p(r), \tag{2.19}$$

where ϕ_s and ϕ_p have the same meaning as in Eq. (2.16). Then the factor $(\mu_{c\tau,v\sigma}\cdot\mu_{v\sigma',c\tau'})$ in Eq. (2.12) can be written in the 8×8 matrix representation as

$$(\mu_{c\tau,v\sigma}\cdot\mu_{v\sigma',c\tau'})=\begin{pmatrix} |\alpha v_1\rangle & |\alpha v_2\rangle & |\alpha v_3\rangle & |\alpha v_4\rangle & |\beta v_1\rangle & |\beta v_2\rangle & |\beta v_3\rangle & |\beta v_4\rangle \\ 1 & 0 & 0 & 0 & 0 & \sqrt{\frac{1}{3}} & 0 & 0 \\ 0 & \frac{2}{3} & 0 & 0 & 0 & 0 & \frac{2}{3} & 0 \\ 0 & 0 & \frac{1}{3} & 0 & 0 & 0 & 0 & \sqrt{\frac{1}{3}} \\ 0 & 0 & 0 & 0 & 0 & 0 & 0 & 0 \\ 0 & 0 & 0 & 0 & 0 & 0 & 0 & 0 \\ \sqrt{\frac{1}{3}} & 0 & 0 & 0 & 0 & \frac{1}{3} & 0 & 0 \\ 0 & \frac{2}{3} & 0 & 0 & 0 & 0 & \frac{2}{3} & 0 \\ 0 & 0 & \sqrt{\frac{1}{3}} & 0 & 0 & 0 & 0 & 1 \end{pmatrix}\cdot 2\mu^2\ . \tag{2.20}$$

As can be guessed from Eq. (2.18), the second term of the long-range exchange energy in Eq. (2.12) has a form given by

$$H_{exch}^{LR(2)} = \begin{pmatrix} |\alpha v_1\rangle & |\alpha v_2\rangle & |\alpha v_3\rangle & |\alpha v_4\rangle & |\beta v_1\rangle & |\beta v_2\rangle & |\beta v_3\rangle & |\beta v_4\rangle \\ * & * & * & 0 & 0 & * & * & * \\ * & * & * & 0 & 0 & * & * & * \\ * & * & * & 0 & 0 & * & * & * \\ 0 & 0 & 0 & 0 & 0 & 0 & 0 & 0 \\ 0 & 0 & 0 & 0 & 0 & 0 & 0 & 0 \\ * & * & * & 0 & 0 & * & * & * \\ * & * & * & 0 & 0 & * & * & * \\ * & * & * & 0 & 0 & * & * & * \end{pmatrix}, \tag{2.21}$$

where * indicates a nonzero block matrix whose dimension is given by the number of the envelope function bases. Similar matrix representations of the exciton exchange interaction in QW's were discussed by Maialle *et al.*[19]

Here we consider localized excitons at quantum-dot-like islands in QW structures which are formed by the lateral fluctuations of the QW thickness. In these islandlike structures, the confinement in the direction of the crystal growth is strong, whereas the confinement in the lateral direction is rather weak. Furthermore, the island structures were found to be elongated along the $[1\bar{1}0]$ direction.[5] Thus these island structures can be modeled by an anisotropic quantum disk. In order to facilitate the calculation, the lateral confinement potential in the x and y directions is assumed to be Gaussian as

$$v_{e(h)}(r) = v_{e(h)}^0 \exp\left[-\left(\frac{x}{a}\right)^2 - \left(\frac{y}{b}\right)^2\right], \tag{2.22}$$

where the lateral size parameters a and b can be fixed in principle from the measurement of morphology by, e.g., STM but the actual size would be different from the morphological size because of the presence of the surface depletion layer and so on. Thus the parameters a and b are left as adjustable parameters. The exciton envelope function in such an anisotropic quantum disk can be approximated as

$$\begin{aligned} f(r_e, r_h) = & \sum_{l_e, l_h, m_e, m_h} C(l_e, l_h, m_e, m_h) \\ & \times \left(\frac{x_e}{a}\right)^{l_e} \left(\frac{x_h}{a}\right)^{l_h} \left(\frac{y_e}{b}\right)^{m_e} \left(\frac{y_h}{b}\right)^{m_h} \cdot \exp\left[-\frac{1}{2}\left\{\left(\frac{x_e}{a}\right)^2 + \left(\frac{x_h}{a}\right)^2 + \left(\frac{y_e}{b}\right)^2 + \left(\frac{y_h}{b}\right)^2\right\} - \alpha_x (x_e - x_h)^2 \right. \\ & \left. - \alpha_y (y_e - y_h)^2\right] \varphi_0(z_e) (\varphi_0(z_h) \text{ or } \varphi_1(z_h)) \end{aligned} \tag{2.23}$$

with

$$\varphi_0(z) = \sqrt{\frac{2}{L_z}} \cos\left(\frac{\pi z}{L_z}\right),$$

$$\varphi_1(z) = \sqrt{\frac{2}{L_z}} \sin\left(\frac{2\pi z}{L_z}\right), \tag{2.24}$$

where $C(l_e, l_h, m_e, m_h)$ is the expansion coefficient, L_z the QW thickness, the factor 1/2 in the exponent is attached to make the probability distribution $|f(r_e, r_h)|^2$ to follow the functional form of the confining potential and α_x and α_y indicate the degree of the electron-hole correlation and are determined variationally. Concerning the envelope function in the z-direction, the lowest two functions are taken into account for the hole to guarantee sufficient accuracy. The electron-hole relative motion within the exciton state is not much different from that in the bulk because the lateral confinement is rather weak. As a result, the parameters α_x and α_y are weakly dependent on the lateral size. Because of the inversion symmetry of the confining potential, the parity is a good quantum number and the wavefunction can be classified in terms of the combination of parities of $x^{l_e+l_h}$, $y^{m_e+m_h}$ and φ_0 or φ_1. In actual calculations, terms up to the sixth power are included, namely, $0 \leqslant l_e + l_h$, $m_e + m_h \leqslant 6$ to ensure the convergence of the calculation. The potential depth for the lateral motion of the electron and the hole can be guessed from the splitting energies of the exciton states due to the monolayer fluctuation of the QW thickness. The value of $|v_e^0 - v_h^0|$ is typically about 10 meV for the nominal QW thickness about 3 nm.[1] Of course, even if $v_e^0 - v_h^0$ is fixed, each value of v_e^0 and v_h^0 cannot be determined uniquely. Here we employ $v_e^0 = -6$ meV and $v_h^0 = 3$ meV in most parts of this paper, referring to the experimental results on the exciton energy spectra and assuming $|v_e^0| : |v_h^0| = 2:1$, but we will later examine several cases of the potential depth.

It is important to examine the size-dependence of the exchange energy. For that purpose, we note first of all that

$$f(r_e, r_h) \propto 1/L^3(\text{quantum dot}), 1/L^2(\text{quantum disk}), \tag{2.25}$$

where L is the characteristic size of a quantum dot or the lateral size of a quantum disk with a fixed disk height. This scaling comes simply from the normalization

$$\int d^3r_e \int d^3r_h \ |f(r_e,r_h)|^2 = 1. \tag{2.26}$$

Then the short-range exchange term in Eq. (2.13) scales as

$$L^3 \frac{1}{L^3}\frac{1}{L^3} \propto \frac{1}{L^3} \ \text{(quantum dot)},$$

$$L^2 \frac{1}{L^2}\frac{1}{L^2} \propto \frac{1}{L^2} \ \text{(quantum disk)}, \tag{2.27}$$

where the first factor L^3 or L^2 comes from the volume integral. The first term of the long-range exchange energy in Eq. (2.12) has the same size-dependence. In the second term of the long-range exchange energy, the operator div and $1/|r-r'|$ give rise to a factor of $1/L$ and the integral in Eq. (2.12) scales as

$$L^3 \ \frac{1}{L}\ \frac{1}{L^3}\ \frac{1}{L}\ L^3 \ \frac{1}{L}\ \frac{1}{L^3} \propto \frac{1}{L^3} \ \text{(quantum dot)},$$

$$L^2 \ \frac{1}{L}\ \frac{1}{L^2}\ \frac{1}{L}\ L^2 \ \frac{1}{L}\ \frac{1}{L^2} \propto \frac{1}{L^3} \ \text{(quantum disk)}. \tag{2.28}$$

Thus the exchange energy in quantum dots scales as $1/L^3$ for both the short-range and the long-range parts. On the other hand, in quantum disks, the short-range and the long-range parts of the exchange energy depend on the size differently as $1/L^2$ and $1/L^3$, respectively. Of course, this size-dependence will hold asymptotically only in the strong confinement regime. In general, details of the envelope function are substantially dependent on the size through, for example, the variational parameters α_x and α_y, leading to possible deviation from the rough scaling laws estimated above.

It is important to note that the long-range part of the electron-hole exchange interaction is not absent for the odd-parity exciton states. For these exciton states,

$$\int d^3r \ \ f(r,r) = 0 \tag{2.29}$$

and the oscillator strength vanishes. However, the integrals in Eq. (2.12) do not vanish in general.

III. EXCITON DOUBLET STRUCTURES

Now we discuss the schematic exciton energy level structures in an anisotropic quantum disk as shown in Fig. 1. The conduction band levels are doubly degenerate due to the spin degree of freedom. The valence band levels are also doubly degenerate owing to the Kramers theorem in the absence of a magnetic field even when the valence band mixing is taken into account. Thus each exciton state is fourfold degenerate in the absence of the electron-hole exchange interaction (left column). When the short-range exchange term is included (middle column), the quadruplet is split into two doublets.

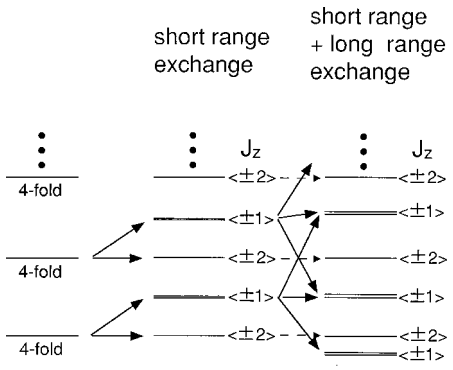

FIG. 1. Exciton energy level structures in an anisotropic quantum dot are shown schematically for the cases with no exchange interaction (left column), with only the short-range exchange interaction (middle column) and with both of the short-range and the long-range exchange interactions (right column).

The first doublet consists of almost degenerate levels which are mainly composed of states having the z-component of the total angular momentum J_z of 2 and -2, namely $|\tau\sigma\rangle = |\alpha v_4\rangle$ or $|\beta v_1\rangle$ in Eq. (2.1) and is denoted as $<\pm 2>$ in Fig. 1. Another doublet is mainly composed of the states having the J_z-component of -1, 0 and 1 and is denoted as $\langle \pm 1\rangle$. This doublet is split slightly by the short-range exchange term. When the long-range exchange term is added (right column), the levels denoted by $\langle \pm 2\rangle$ remain almost the same because the exchange interactions are absent for the $J_z = \pm 2$ states. On the other hand, the levels denoted by $\langle \pm 1\rangle$ are affected rather strongly due to the mixing among themselves. Namely, the doublet splitting increases and the lowest doublet is pushed down by the exchange interaction with excited exciton states. This level restructuring is depicted by solid arrows in Fig. 1. As a result, the exciton ground state can become an optically active state depending on the magnitude of the long-range exchange energy.

This schematic understanding can be confirmed by numerical calculations in which we employ a quantum disk model to simulate a localized exciton in a QW island. In the following, material parameters of GaAs (Ref. 20) are employed (see Appendix for details). The chosen size parameters in Eq. (2.23) are $a = 20$ nm, $b = 15$ nm, and $L_z = 3$ nm. The exciton level structure is shown in Fig. 2 for the case in which only the short-range exchange energy is included. The exciton ground state is optically dark and the first optically active exciton doublet is lying about 0.3 meV above the exciton ground state. The splitting energy of the first optically active exciton doublet is much smaller than the observed splitting. Also for the higher-lying exciton doublets the splitting energy is very small (<1 μeV). On the other hand, when both the short-range and the long-range exchange terms are included as shown in Fig. 3, the exciton ground state is optically active and its doublet splitting is 29 μeV in agreement with experiments.[5] The optically dark exciton states are mainly composed of the $J_z = \pm 2$ components and its first doublet is lying about 0.8 meV above the exciton ground state. Thus the long-range exchange term is important to understand the experimental results. So far we have considered the even-parity exciton states which include both the optically active and the dark states. In addition to these, there are odd-parity exciton states, all of which are optically

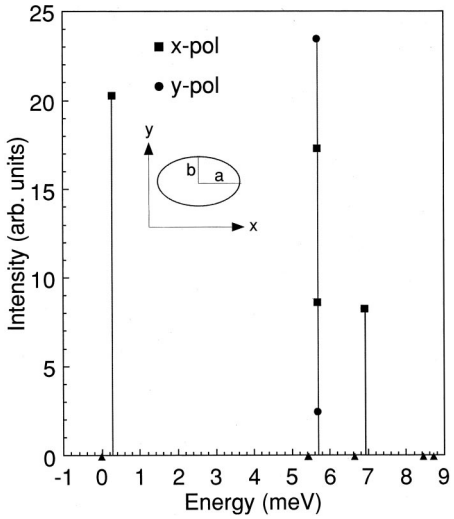

FIG. 2. Exciton energy level structures are shown for a GaAs elliptical quantum disk with the size parameters $a=20$ nm, $b=15$ nm and L_z(disk height)$=3$ nm, in which only the short-range exchange term is taken into account. The $x(y)$-direction of the polarization is along the semimajor (semiminor) axis of the potential ellipse. For the first and the fourth doublets, the energy position and the intensity are almost degenerate. The triangles indicate the energy positions of the even-parity dark states.

dark. They are plotted by diamonds in Fig. 3 to show their energy positions. They do not contribute to the luminescence but would play the role as the intermediate states of relaxation processes as will be discussed in Sec. VI.

Furthermore, the importance of the long-range exchange interaction can be seen in the dependence of the doublet splitting energy on the aspect ratio of the confinement potential ellipse. The variation of the doublet splitting energy is shown in Fig. 4 for the lowest three optically active exciton doublets when the semimajor axis length a is fixed at 20 nm and the semiminor axis length b is varied around 20 nm with a fixed value of $L_z=3$ nm. When the potential ellipse approaches a circular shape, the doublet splitting energy decreases to zero. This demonstrates the sensitivity of the long-range exchange interaction to the quantum disk shape and its significance in determining the doublet splitting.

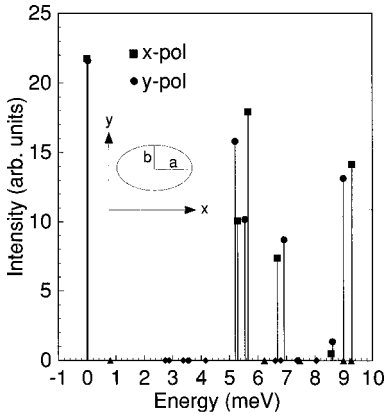

FIG. 3. Exciton energy level structures are shown for a GaAs elliptical quantum disk with the size parameters $a=20$ nm, $b=15$ nm and L_z(disk height)$=3$ nm, in which both of the short-range and the long-range exchange terms are taken into account. The meaning of the $x(y)$-direction and the triangles are the same as in Fig. 2. The diamonds indicate the energy positions of the odd-parity exciton states.

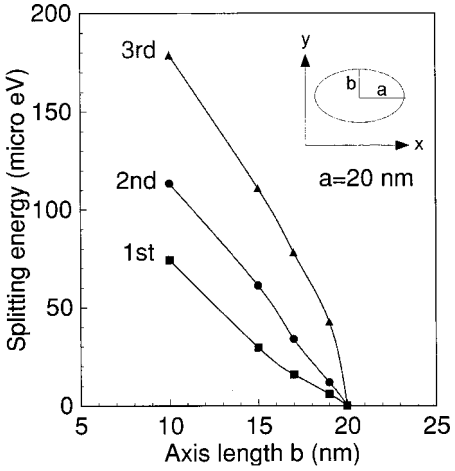

FIG. 4. The variation of the doublet splitting energy in a GaAs elliptical quantum disk is shown for the lowest three optically active exciton doublets when the semimajor axis length a is fixed at 20 nm and the semiminor axis length b is varied around 20 nm with a fixed value of $L_z=3$ nm.

We have examined the dependence of the doublet splitting energy on the size of a quantum disk with a fixed aspect ratio a/b. The results are shown in Fig. 5 for $a/b=4/3$. The size-dependence of the doublet splitting energy for the lowest doublet is rather weak, suggesting that the exciton wavefunction is localized in the interior of the confinement potential and is not strongly affected by the potential size. On the other hand, for the higher-lying exciton doublets, the splitting energy shows a dependence of $1/a^n(n=1.3\sim1.5)$ as depicted by solid lines in Fig. 5. A simple argument based on Eqs. (2.27) and (2.28) indicates the $1/a^2$ dependence for the short-range exchange term and the $1/a^2$ or $1/a^3$ dependence for the long-range exchange term. The calculated size-dependence is deviating from these simple predictions. As mentioned before, this deviation might be ascribed to the size-dependence of details of the exciton wavefunctions.

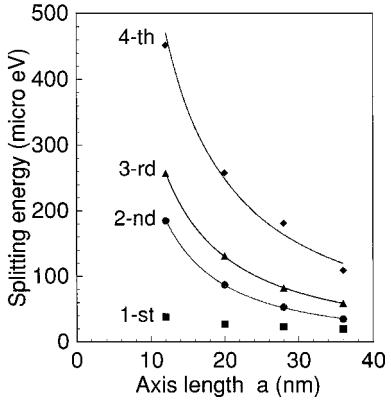

FIG. 5. The doublet splitting energy in a GaAs elliptical quantum disk is plotted for the lowest four exciton doublets as a function of the semimajor axis length a with a fixed aspect ratio $a/b=4/3$ and a fixed value of $L_z=3$ nm. The solid lines show a dependence of $1/a^n(n=1.3\sim1.5)$.

So far we have employed the values of $v_e^0 = -6$ meV and $v_h^0 = 3$ meV for the lateral confinement potential in Eq. (2.22). We examined, however, the dependence of the doublet splitting energy on the potential depth. The splitting energy of the ground exciton doublet is 27 μeV for $(v_e^0, v_h^0) = (-4$ meV, 2 meV), 29 μeV for $(v_e^0, v_h^0) = (-6$ meV, 3 meV), 34 μeV for $(v_e^0, v_h^0) = (-9$ meV, 4 meV) and 46 μeV for $(v_e^0, v_h^0) = (-15$ meV, 10 meV). The trend of these numerical results can be understood as follows. When the lateral confinement is strengthened, both of the electron and the hole wavefunctions shrink spatially and the overlap between them increases, resulting in the increase of both the short-range and the long-range exchange interactions and the enhancement of the doublet splitting energy.

IV. POLARIZATION CHARACTERISTICS OF EXCITON DOUBLETS

The polarization characteristics of exciton doublets are quite interesting and reveal an important physical aspect. For the lowest doublet, the lower exciton state is polarized along the *x*-direction, namely along the semimajor axis of the potential ellipse. On the other hand, the upper exciton state is polarized along the *y*-direction (the semiminor axis). However, for the second and third doublets the relation between the energetic order and the polarization direction is reversed. According to our calculation, the polarization direction of the lower exciton state is *x*, *y*, *y*, and *x* for the lowest four exciton doublets in complete agreement with the experiment.[5] These features can be understood in view of the spatial distribution of exciton polarization.

The transition dipole moment of an exciton state is given by

$$P_i = \sum_r \sum_{\tau,\sigma} \langle c\tau|\mu_i|v\sigma\rangle \ f^*_{\tau\sigma}(r,r), \quad (i=x,y,z), \quad (4.1)$$

where μ_i is the dipole moment operator in the *i*-direction. In the following we interpret $\Sigma_{\tau,\sigma}\langle c\tau|\mu_i|v\sigma\rangle f^*_{\tau\sigma}(r,r)$ as the polarization density in the *i*-direction at the position *r*. But this quantity is in general complex and we consider the absolute value to understand the qualitative features. The polarization distribution calculated in this way is shown in Fig. 6 for the first exciton doublet in a confinement potential with $(a,b) = (20$ nm, 15 nm). For the lower exciton state (1 state), the distribution function of the *x*-polarization is single-peaked [Fig. 6(a)] corresponding to a uniform distribution of the polarization direction. On the other hand, the distribution function of the *y*-polarization [Fig. 6(b)] is four-peaked, indicating a staggered distribution of the polarization direction. For the upper exciton state of the first doublet ($1'$ state), the spatial distribution functions of the *x*- and *y*-polarization [Figs. 6(c) and 6(d)] are interchanged relative to the case of the lower exciton state. These features of polarization distribution are schematically depicted in Figs. 7(a)–7(d).

Now we consider the dipole-dipole interaction originating from the long-range exchange interaction. The dipole-dipole interaction energy changes its sign according to the polarization configuration as shown in Fig. 8. Then we see that for the *x*-polarized exciton state (1 state) the negative contribution is significant, whereas for the *y*-polarized exciton state ($1'$ state) the positive contribution is substantial. For the staggered configuration of polarizations like in Figs. 7(b) and 7(c), the positive and negative dipole-dipole interactions largely canceled each other and the resultant contribution was rather small compared to that from Figs. 7(a) and 7(d). As a consequence, the *x*-polarized exciton state has a lower energy than the *y*-polarized state.

The same argument can be extended to the higher-lying doublet states. The distribution functions of the *x*- and *y*-polarization are depicted in Figs. 9, 10, and 11 for the second, third, and fourth exciton doublets, respectively. For the *n*th doublet, the exciton levels are named as *n* and n' corresponding to the *x*- and *y*-polarized state, respectively. In the excited states, the number of nodes of the exciton wavefunction increases and correspondingly the polarization distribution becomes more staggered and complicated. For the second and third doublets, there are two nodes in the *x*-direction, whereas for the fourth doublet there are two nodes in the *y*-direction. These polarization distribution functions are schematically depicted in Figs. 12, 13, and 14. The sign of the dipole-dipole interaction energy deduced from Fig. 8 are also given in the figures. Then we see that for the second and third doublets the *y*-polarized state ($2'$ or $3'$ state) is energetically lower than the *x*-polarized state (2 or 3 state). On the other hand, for the fourth doublet the energy of the *x*-polarized state (4 state) is lower than that of the *y*-polarized state ($4'$ state). Thus the key concepts to understand the energetic order of the orthogonally polarized exciton doublet states are the node configuration of the polarization distribution and the dipole-dipole interaction originating from the long-range exchange term.

We have examined the dependence on the lateral size of the quantum disk of the energetic order of the orthogonally polarized exciton doublet states. For the quantum disks with a fixed aspect ratio, namely $a/b = 4/3$, we examined the cases of $(a,b) = (12$ nm, 9 nm), (20 nm, 15 nm), (28 nm, 21 nm) and (36 nm, 27 nm) with a fixed disk height of $L_z = 3$ nm and found that the polarization direction of the lower exciton state of the lowest four exciton doublets is commonly *x*, *y*, *y*, and *x*. This reflects the same node configuration of the exciton polarization for these quantum disks having the common value of the aspect ratio.

We examined also the cases with different aspect ratios, namely the cases of $(a,b) = (30$ nm, 10 nm) and (40 nm, 10 nm). The polarization direction of the lower exciton state of the lowest four exciton doublets is *x*, *y*, *y*, and *y* for $(a,b) = (30$ nm, 10 nm) and *x*, *x*, *y*, and *y* for $(a,b) = (40$ nm, 10 nm), respectively. These features can be understood by inspecting the polarization distribution functions, although they are not shown. Thus the polarization characteristics of the exciton doublet states depend sensitively on the aspect ratio of the lateral confinement potential.

V. POLARIZATION RELAXATION OF EXCITONS

Now we discuss the polarization relaxation by the electron-phonon interaction. In this system the relevant energy level spacings are about a few meV and thus we take into account only the interactions with acoustic phonons through the deformation potential coupling and the piezoelectric coupling.[21,11] The electron-phonon interaction itself

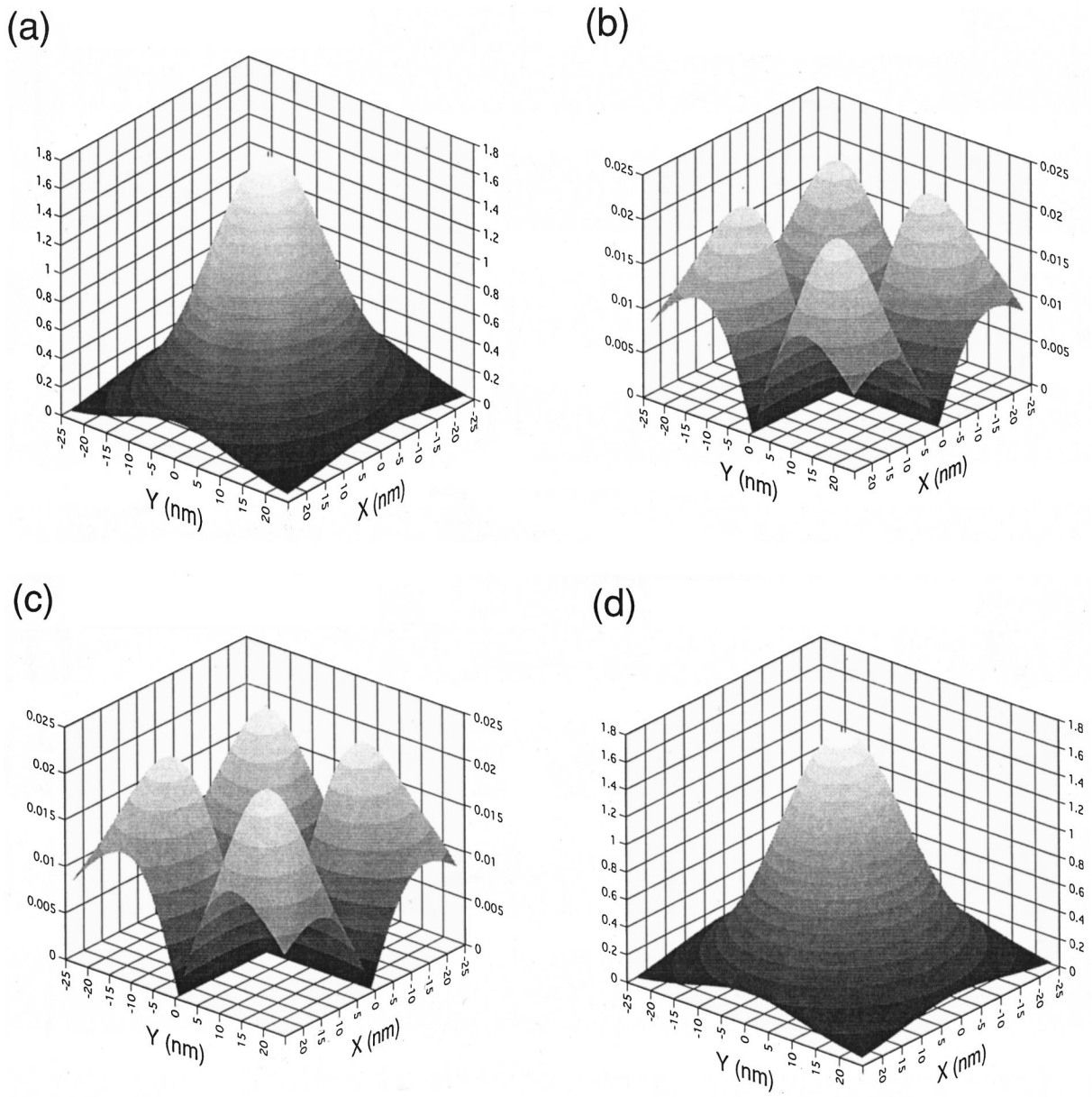

FIG. 6. The polarization distribution function is plotted for the first exciton doublet states in a GaAs elliptical quantum disk with the size parameters $a=20$ nm, $b=15$ nm, and L_z(disk height)$=3$ nm. (a) x-polarization distribution for the x-polarized exciton state (1 state), (b) y-polarization distribution for the 1 state, (c) x-polarization distribution for the y-polarized exciton state ($1'$ state), (d) y-polarization distribution for the $1'$ state. The weight (z-axis) is plotted in the arbitrary units but its scale is common for all the cases.

does not flip the electron spins. The exciton eigenstates are mixed states of all the eight combinations of the Bloch functions as in Eq. (2.1). Thus it is possible to make a transition between the dominantly x-polarized states and the dominantly y-polarized states through the electron-phonon interaction.

For the inter-doublet transitions, it is sufficient to consider only the one-phonon processes because the acoustic phonons

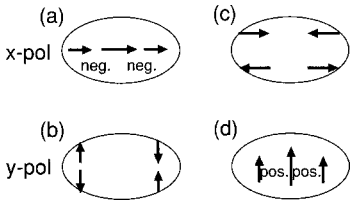

FIG. 7. Schematic representation of the polarization distribution in Fig. 6 for the first exciton doublet. (a) x-polarization distribution for the 1 state, (b) y-polarization distribution for the 1 state, (c) x-polarization distribution for the $1'$ state, (d) y-polarization distribution for the $1'$ state.

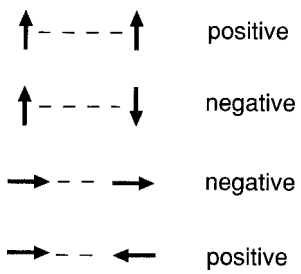

FIG. 8. The sign of the dipole-dipole interaction energy for various configurations of polarization direction.

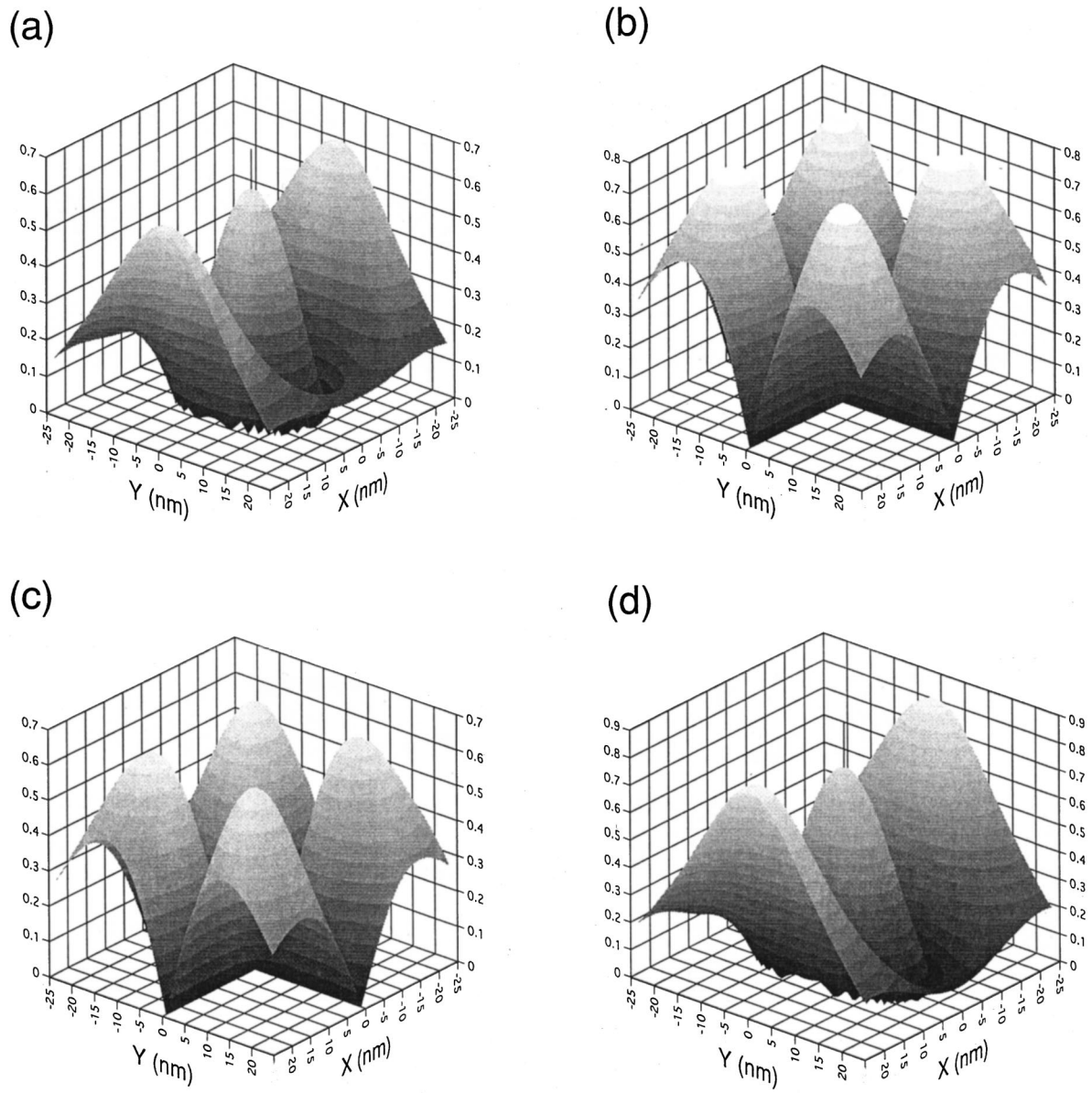

FIG. 9. The polarization distribution function is plotted for the second exciton doublet states in the same GaAs elliptical quantum disk as in Fig. 6. (a) *x*-polarization distribution for the *x*-polarized state (2 state), (b) *y*-polarization distribution for the 2 state, (c) *x*-polarization distribution for the *y*-polarized state ($2'$ state), (d) *y*-polarization distribution for the $2'$ state.

resonant with the relevant transition energy have a wavelength comparable to the quantum disk size and the matrix element of the electron-phonon interaction has a sizable magnitude. On the other hand, for the intra-doublet transitions, we have to consider multiphonon, at least two-phonon processes because the contribution from the one-phonon processes is vanishingly small. In general, the matrix element of the electron-phonon interaction is proportional to

$$\int d^3r_e \int d^3r_h \; F_f^*(r_e,r_h)e^{i\vec{q}\vec{r}_e} \;(\text{or } e^{i\vec{q}\vec{r}_h})F_i(r_e,r_h), \tag{5.1}$$

where $\vec{q}$ is the phonon wavevector and $F_i(F_f)$ is the envelope function of the initial (final) exciton state. Since the doublet splitting energy is about several tens of μeV, the corresponding wavevector of phonons is rather small ($\sim 10^5$ cm^{-1}) and we can approximate as

$$\int d^3r_e \int d^3r_h \; F_f^*(r_e,r_h)\left(1+i\vec{q}\cdot\vec{r}_e(i\vec{q}\cdot\vec{r}_h) + \frac{1}{2}(i\vec{q}\cdot\vec{r}_e)^2((i\vec{q}\cdot\vec{r}_h)^2)+\cdots\right)F_i(r_e,r_h)$$
$$= \int d^3r_e \int d^3r_h \; F_f^*(r_e,r_h) \times\left(\frac{1}{2}(i\vec{q}\cdot\vec{r}_e)^2((i\vec{q}\cdot\vec{r}_h)^2)+\cdots\right)F_i(r_e,r_h), \tag{5.2}$$

where the first term in the parentheses of the first line vanishes due to the orthogonality of the eigenfunctions and the second term also vanishes because the parity is a good quantum number for the confinement potential with inversion

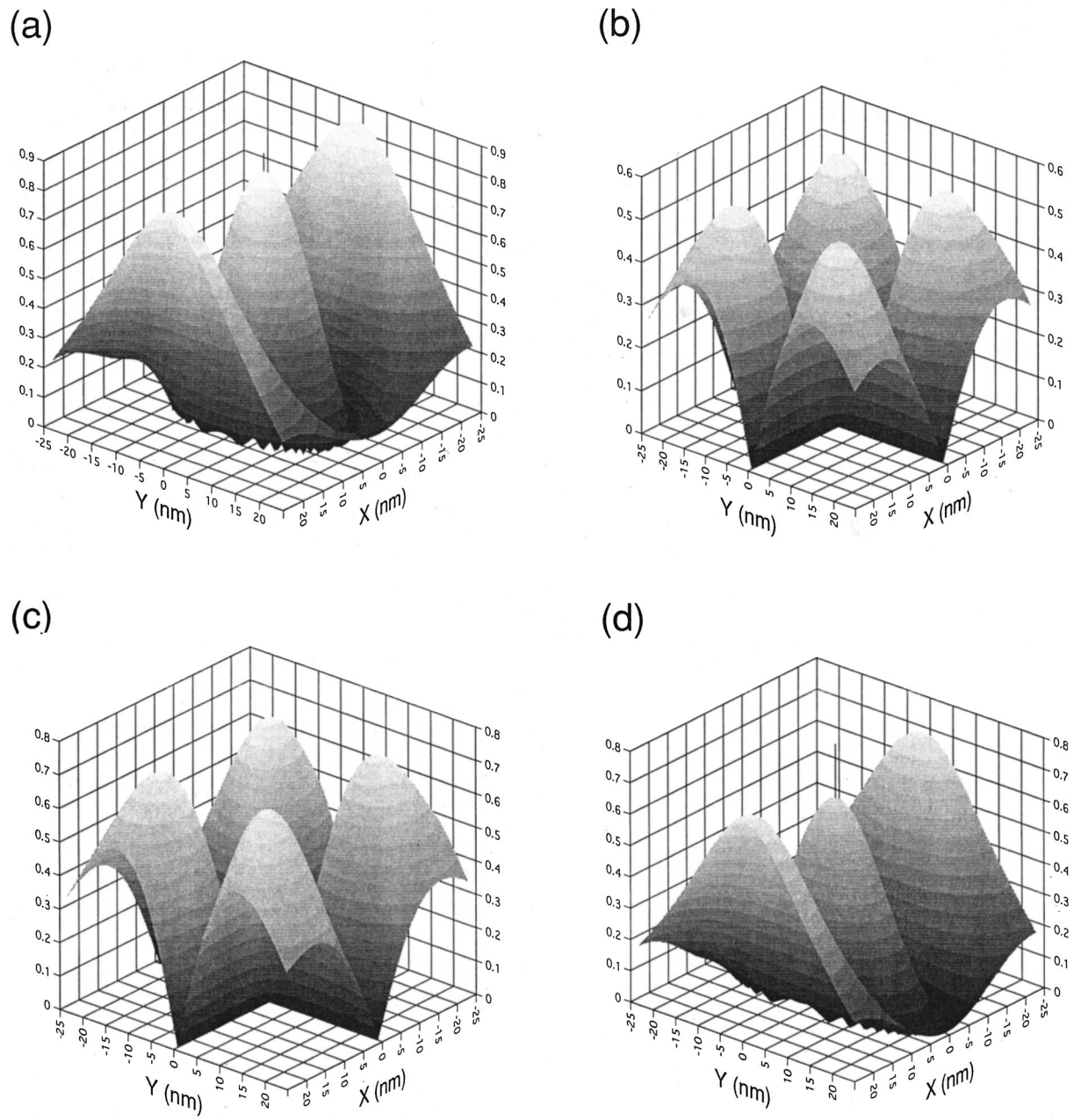

FIG. 10. The polarization distribution function is plotted for the third exciton doublet states in the same GaAs elliptical quantum disk as in Fig. 6. (a) *x*-polarization distribution for the *x*-polarized state (3 state), (b) *y*-polarization distribution for the 3 state, (c) *x*-polarization distribution for the *y*-polarized state (3′ state), (d) *y*-polarization distribution for the 3′ state.

symmetry. As a result, the probability of one-phonon processes is rather small and we have to consider two-phonon processes. The probability of the Raman-type two-phonon processes is given by

$$\sum_{\omega_1,\omega_2}\left|\sum_j \frac{\langle f|H_{e-ph}(\omega_2)|j\rangle\langle j|H_{e-ph}(\omega_1)|i\rangle}{E_i-E_j\mp\hbar\omega_1}\right|^2 \times\delta(E_f-E_i\pm\hbar\omega_1\mp\hbar\omega_2), \tag{5.3}$$

where H_{e-ph} is the electron-phonon interaction, j denotes the intermediate exciton states and the summation over the energies (ω_1,ω_2) and the wave vectors of two phonons is carried out. In Table I, the calculated transition rates at 30 K of the one-phonon and the two-phonon processes are compared for the intra-doublet transitions of the lowest four exciton doublets. It can be confirmed that the two-phonon processes are dominantly contributing.

Combining the one-phonon and the two-phonon processes, the calculated relaxation times at 30 K are shown in Fig. 15 for the lowest four exciton doublet states having the even parity. In this figure the dark exciton states consisting of the even-parity dark states and the odd-parity states are not included. The relaxation time within each exciton doublet states is rather long and about several nanoseconds because of the small energy difference. These relaxation times are not inconsistent with a recent measurement on InGaAs QD.[13] On the other hand, the typical relaxation times within exciton states having the same polarization (*x*- or *y*-polarization) are about 100 ps. These relaxation times are

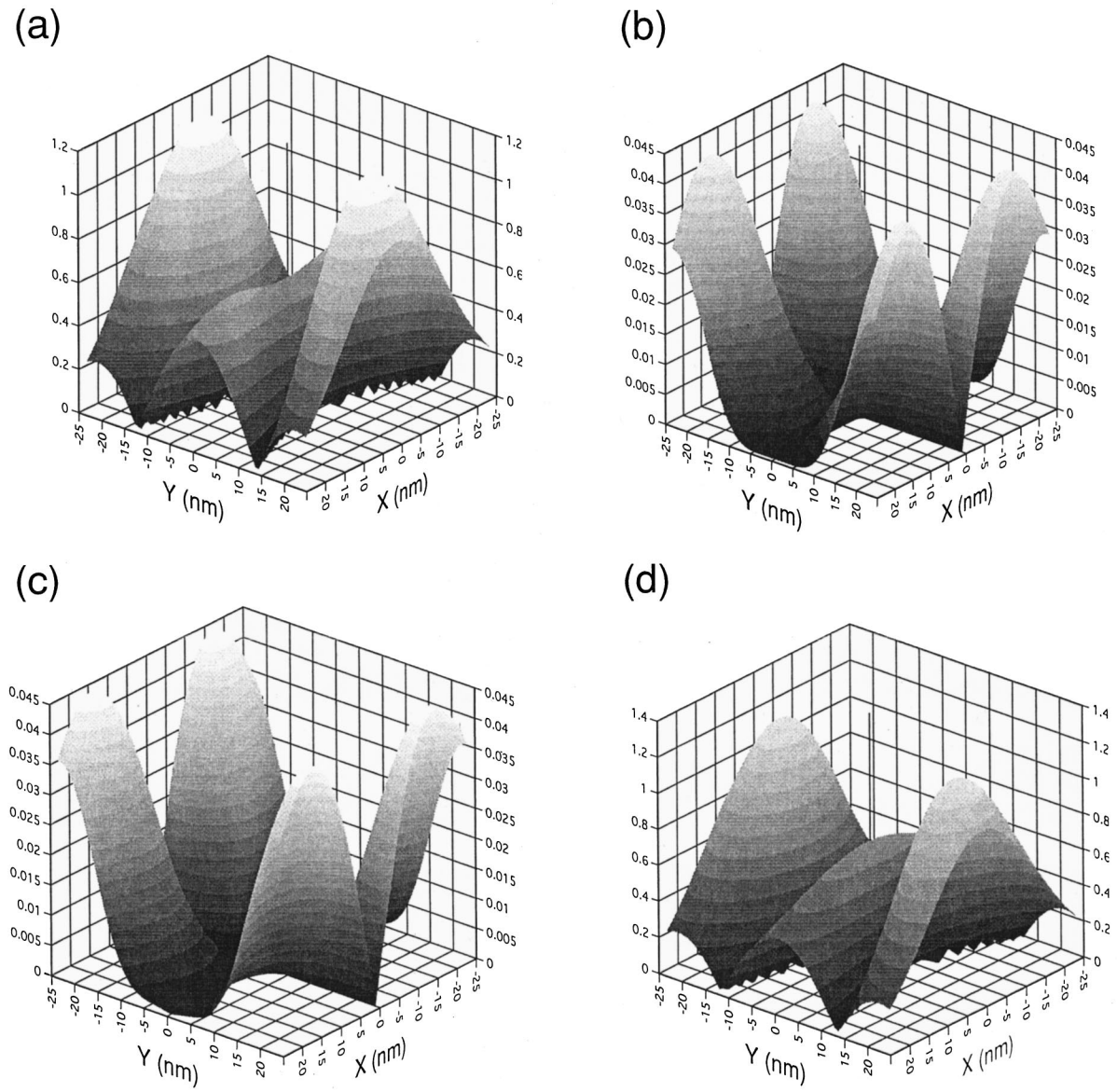

FIG. 11. The polarization distribution function is plotted for the fourth exciton doublet states in the same GaAs elliptical quantum disk as in Fig. 6. (a) *x*-polarization distribution for the *x*-polarized state (4 state), (b) *y*-polarization distribution for the 4 state, (c) *x*-polarization distribution for the *y*-polarized state ($4'$ state), (d) *y*-polarization distribution for the $4'$ state.

in good agreement with the recently measured values[12] using the single-dot pump-probe spectroscopy.

The relaxation time from the third exciton level to the second exciton level is rather long for both the *x*- and the *y*-polarized states, reflecting the small energy difference between the second and the third exciton levels (< 1 meV). This is explained by the same argument given at Eq. (5.2). It is to be noted that the inset in Fig. 15 shows the exciton level structures only schematically and does not reflect the actual level spacings accurately. The relaxation time from the second exciton level to the exciton ground state is about 100 ps, whereas that from the third exciton level to the exciton ground state is about several tens of picoseconds. Thus the relaxation from the third exciton level to the exciton ground state occurs directly instead of the two-step sequence through the second exciton state. In general, the transition between exciton levels whose energy difference is small would be often bypassed by some other efficient relaxation paths. This kind of phenomenon seems to have been observed experimentally.[22]

Now we discuss the cross-relaxation or polarization relaxation between exciton states having the mutually orthogonal polarizations. The calculated results at 30 K are given in Fig. 16. The cross-relaxation times are of the same order of magnitude as the relaxation times within the exciton states having the same polarization. Thus the polarization relaxation of excitons occurs rather efficiently. At the same time, it is to be noted that the cross-relaxation rate is rather small for the transition between the third and the second exciton states having the orthogonal polarizations. This is also caused by the small energy difference.

The temperature dependence of the relaxation rate is related to the number of phonons involved in the transition. In the case of one-phonon processes, the relaxation rate is proportional to the phonon occupation number which can be approximated as

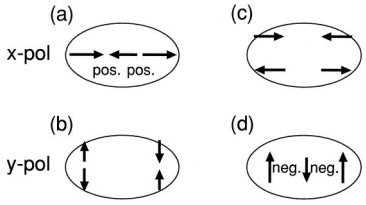

FIG. 12. Schematic representation of the polarization distribution in Fig. 9 for the second exciton doublet. (a) *x*-polarization distribution for the 2 state, (b) *y*-polarization distribution for the 2 state, (c) *x*-polarization distribution for the $2'$ state, (d) *y*-polarization distribution for the $2'$ state.

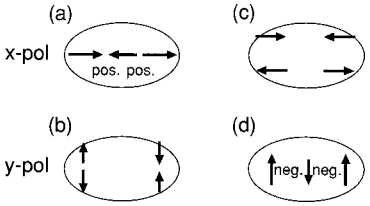

FIG. 13. Schematic representation of the polarization distribution in Fig. 10 for the third exciton doublet. (a) *x*-polarization distribution for the 3 state, (b) *y*-polarization distribution for the 3 state, (c) *x*-polarization distribution for the $3'$ state, (d) *y*-polarization distribution for the $3'$ state.

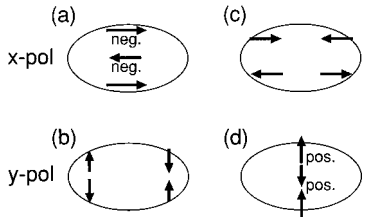

FIG. 14. Schematic representation of the polarization distribution in Fig. 11 for the fourth exciton doublet. (a) *x*-polarization distribution for the 4 state, (b) *y*-polarization distribution for the 4 state, (c) *x*-polarization distribution for the $4'$ state, (d) *y*-polarization distribution for the $4'$ state.

TABLE I. Comparison between the rates of the one-phonon and the two-phonon processes at 30 K for the intra-doublet transitions of the lowest four exciton doublets in a GaAs elliptical quantum disk with the size parameters $a=20$ nm, $b=15$ nm and L_z(disk height)$=3$ nm.

	1-phonon	2-phonon
$1-1'$	$1.42\cdot10^{-8}\mu$eV	0.071μeV
$2-2'$	0.017	0.156
$3-3'$	0.068	0.418
$4-4'$	0.021	0.227

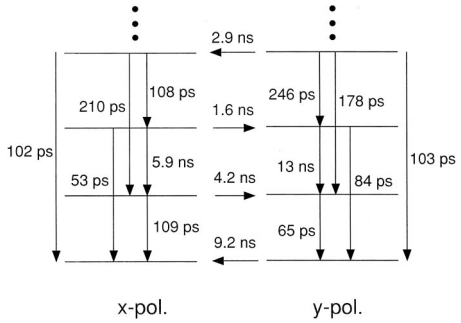

FIG. 15. Population relaxation times at 30 K for the polarization-conserving processes within the lowest four optically active exciton doublet states and for the intra-doublet relaxation processes in a GaAs elliptical quantum disk with the size parameters $a=20$ nm, $b=15$ nm and L_z(disk height)$=3$ nm. It is to be noted that the energy level structures are only schematic and are not reflecting the actual energy spacings.

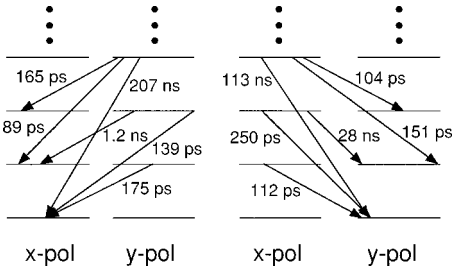

FIG. 16. Polarization relaxation times at 30 K within the lowest four optically active exciton doublet states in the same quantum disk as in Fig. 15.

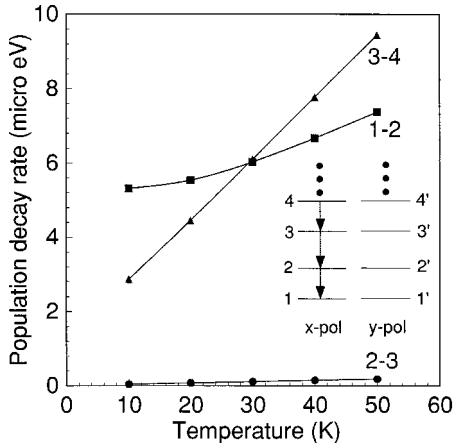

FIG. 17. Population relaxation rates are plotted as a function of temperature for the successive transitions within the *x*-polarized exciton states in the same quantum disk as in Fig. 15.

$$n(\omega)=\frac{1}{e^{\hbar\omega/k_BT}-1}\sim\frac{k_BT}{\hbar\omega} \tag{5.4}$$

at high temperatures, such that $\hbar\omega \ll k_BT$. In Fig. 17, the relaxation rates for a few transitions within the *x*-polarized exciton levels are shown as a function of temperature. Since the energy difference between the second and the third exciton states is rather small, the linear temperature dependence is clearly seen. On the other hand, as mentioned before, the relaxation within the exciton doublet states occurs mainly through two-phonon processes and the rate is typically proportional to a factor given by

$$\sum_{\omega_1,\omega_2} M(\omega_1,\omega_2)n(\omega_1)(1+n(\omega_2)), \tag{5.5}$$

where M contains the matrix elements of the electron-phonon interaction. According to Eq. (5.4), the rate in Eq. (5.5) is expected to be proportional to T^2 at high temperatures. In Fig. 18, the temperature dependence of relaxation rates is shown for the intra-doublet transitions of the lowest four exciton doublets. The T^2-dependence can be confirmed at high temperatures. In fact, in the temperature range from 30 K to 50 K, the calculated results can be fit well by T^n ($n=1.98\sim2.24$).

VI. PHOTOLUMINESCENCE SPECTRUM UNDER SELECTIVE EXCITATION

In the last section, it was found that the polarization relaxation occurs efficiently in our system. In order to see this effect more clearly, we have calculated the photoluminescence spectra under selective excitation. We have so far discussed the even-parity exciton states because the optically active exciton states have the even parity. There are, however, odd-parity exciton states which are optically dark and their energy positions are shown by diamonds in Fig. 3 for a GaAs elliptical quantum disk with the size parameters $a=20$ nm, $b=15$ nm and L_z (disk height)$=3$ nm. The relaxation times within the odd-parity exciton states and those between the even-parity exciton states and the odd-parity exciton states are of the same order of magnitude as the relaxation times within the even-parity exciton states, suggesting that the dark exciton states would play possibly important roles as the intermediate states of relaxation processes. We have formulated a set of rate equations for the occupation probability of relevant exciton levels which include 12 odd-parity and 14 even-parity exciton levels in the ascending order of energy up to 7 meV from the exciton ground state.

The photoluminescence spectrum under the resonant cw excitation is obtained by a stationary solution of the set of rate equations. The results for the *x*-polarized excitation at the fourth exciton level are shown in Fig. 19 for 30 K. The polarization-conserving luminescence from the *x*-polarized exciton ground state is strong but the luminescence from the *y*-polarized exciton ground state has also substantial intensity. The situation is similar also for the resonant cw excitation of the *y*-polarized fourth exciton level as shown in Fig. 20. In this case, however, the luminescence from the *x*-polarized exciton ground state is stronger than that from the *y*-polarized exciton ground state, indicating more efficient relaxation from the *y*-polarized states to the *x*-polarized states than the reverse process. These results indicate clearly the presence of efficient paths of polarization relaxation.

In the same way, we can calculate the excitation spectra of the exciton photoluminescence. The excitation spectra for the detection of luminescence from the *x*-polarized exciton ground state are shown in Fig. 21 for both the *x*- and *y*-polarized excitation. This spectrum is very similar to the absorption spectrum in Fig. 3, although the intensity ratio between the *x*- and the *y*-polarized components is different for the fourth exciton doublet. Similar behaviors can be seen in the excitation spectra for the detection of luminescence from the *y*-polarized exciton ground state as shown in Fig. 22. This indicates that the relaxation processes after photoexcitation are not sensitively dependent on the initial polarization direction because of the presence of efficient polarization relaxation through the excited exciton states and thus the emission intensity from the exciton ground state is grossly determined by the absorption intensity of the exciting light.

VII. SUMMARY

In summary, we identified the origin of exciton doublet structures as the long-range part of the electron-hole exchange interaction which is manifested by the anisotropic shape of quantum dots. The physical origin of the energetic order of the orthogonally polarized exciton states of each doublet is clarified by inspecting the spatial distribution of the exciton polarization. The key concepts to understand the energetic order are the node configuration of the distribution function of exciton polarization and the dipole-dipole interaction energy originating from the long-range electron-hole exchange interaction. We studied the population relaxation and predicted a long relaxation time for the intra-doublet transitions about several ns. We also found that the cross-relaxation between orthogonally polarized exciton states occurs, in general, as efficiently as the population relaxation without the change of the polarization direction.

ACKNOWLEDGMENTS

The author would like to thank Dr. Al. L. Efros for useful discussions at the initial stage of this work.

APPENDIX: PARAMETERS RELATED TO THE ELECTRON-HOLE EXCHANGE ENERGIES

Here the determination of parameters E_X^S in Eq. (2.16) and μ in Eq. (2.19) is discussed. These quantities can be fixed from the singlet-triplet splitting energy Δ_{ST} and the longitudinal-transverse splitting energy Δ_{LT} in bulk materials. In bulk, the exciton state can be written as

$$|X\rangle_K=\frac{1}{\sqrt{N}}\sum_{\tau,\sigma}\sum_{n,m} e^{iKR_m}F_{\tau\sigma}(R_n)\ \ a^\dagger_{c\tau R_n+R_m}a_{v\sigma R_m}|0\rangle, \tag{A1}$$

where K is the center-of-mass wave vector, F the envelope function describing the electron-hole relative motion and the Wannier function representation is used. The electron-hole exchange energy is given by

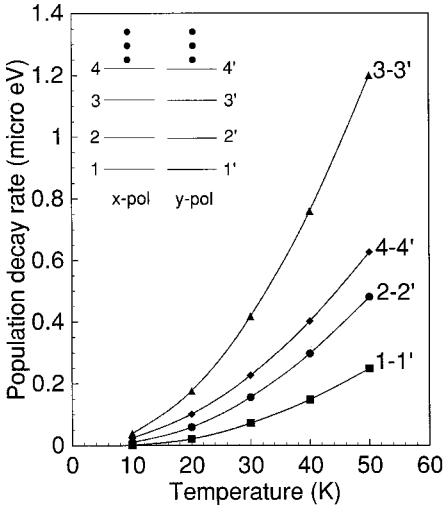

FIG. 18. Polarization relaxation rates are plotted as a function of temperature for the intra-doublet transitions in the same quantum disk as in Fig. 15. The solid lines show a dependence of $T^n(n=1.98\sim2.24)$.

$$\sum_{\tau\sigma\tau'\sigma'} F_{\tau\sigma}(0)F_{\tau'\sigma'}(0)V(c\tau R_0,v\sigma' R_0;c\tau' R_0,v\sigma R_0) + \sum_{\tau\sigma\tau'\sigma'} F_{\tau\sigma}(0)F_{\tau'\sigma'}(0)\sum_{m'\neq m} e^{-iK(R_m-R_{m'})} \times V(c\tau R_m,v\sigma' R_{m'};c\tau' R_{m'},v\sigma R_m), \quad \text{(A2)}$$

where the first(second) term is the short(long)-range exchange term. By the multipole expansion, the second term can be rewritten as

$$-\frac{4\pi}{3v_0}\sum_{\tau\sigma\tau'\sigma'} F_{\tau\sigma}(0)F_{\tau'\sigma'}(0)\,{}^t\vec{\mu}_{c\tau,v\sigma} \times[\hat{1}-3\vec{\hat{K}}{}^t\vec{\hat{K}}]\ \vec{\mu}_{v\sigma',c\tau'}, \quad \text{(A3)}$$

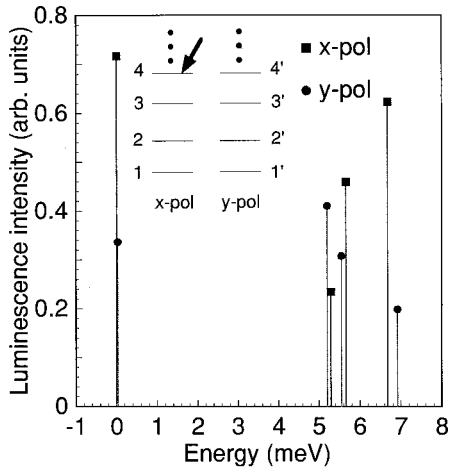

FIG. 19. The photoluminescence spectrum under the resonant cw excitation at the *x*-polarized fourth exciton level at 30 K in a GaAs elliptical quantum disk with the size parameters $a=20$ nm, $b=15$ nm, and L_z(disk height)$=3$ nm.

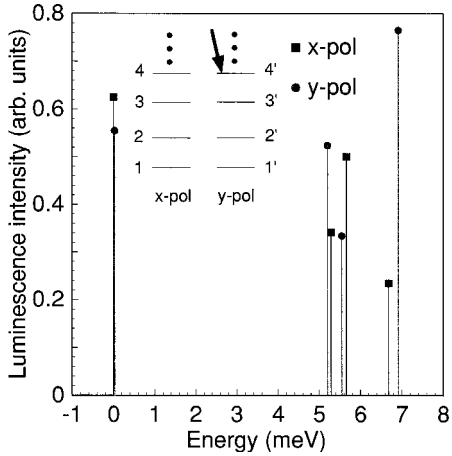

FIG. 20. The photoluminescence spectrum under the resonant cw excitation at the *y*-polarized fourth exciton level at 30 K in the same quantum disk as in Fig. 19.

where $\hat{K}$ is a unit vector in the direction of K. In GaAs the top valence band is the fourfold degenerate $\Gamma_8(J=3/2)$ band. Carrying out a straightforward calculation in the 8×8 matrix form and assuming the ground-state envelope function as

$$F(r)=\sqrt{\frac{v_0}{\pi a_B^3}}\ e^{-r/a_B}, \quad \text{(A4)}$$

where a_B is the exciton Bohr radius and v_0 is the volume of a unit cell, we find the energy level structure as shown in Fig. 23 with

$$E_S=\frac{v_0}{\pi a_B^3}E_X^S \ \text{ and } \ E_L=\frac{4\mu^2}{3a_B^3}. \quad \text{(A5)}$$

The lowest state is the fivefold degenerate $J=2$ dark exciton state, the next lowest state is the doubly degenerate $J=1$

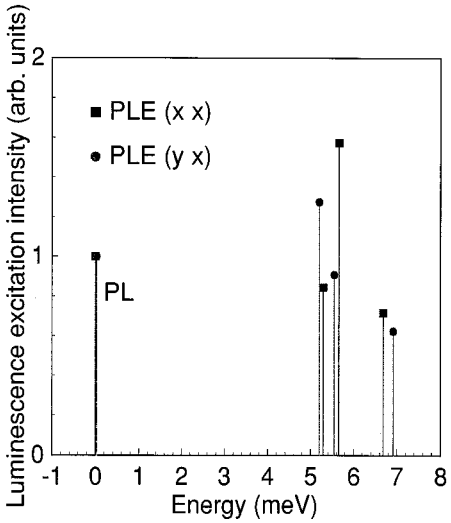

FIG. 21. Photoluminescence excitation spectrum at 30 K under the detection of emission from the *x*-polarized exciton ground state in the same quantum disk as in Fig. 19.

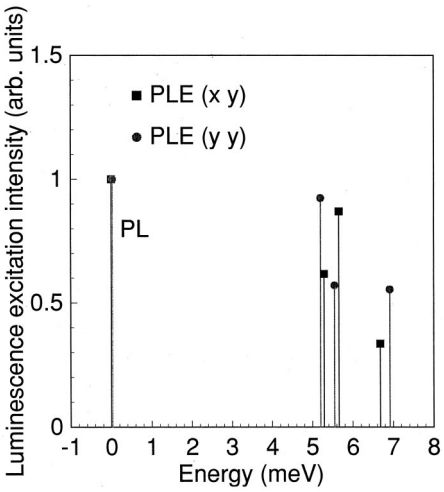

FIG. 22. Photoluminescence excitation spectrum at 30 K under the detection of emission from the *y*-polarized exciton ground state in the same quantum disk as in Fig. 19.

transverse exciton state and the uppermost state is the $J=1$ longitudinal exciton state. Then we can identify as

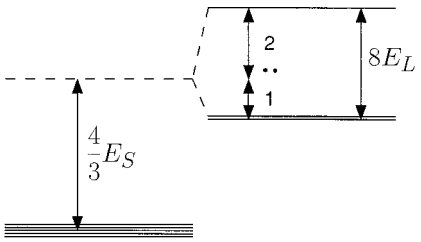

FIG. 23. Schematic level structure of the exciton ground state in bulk materials like GaAs having the fourfold degenerate valence band. The definitions of E_S and E_L are given in the Appendix.

$$\Delta_{ST}=\frac{4v_0}{3\pi a_B^3}E_X^S,\quad \Delta_{LT}=\frac{32\mu^2}{3a_B^3}. \tag{A6}$$

The parameters E_X^S and μ can be fixed from the experimental values of Δ_{ST} and Δ_{LT}.[20] It is to be noted that the subtle problem of screening of the electron-hole exchange interaction is circumvented in the above formulation because the effect of screening is implicitly included in the parameters E_X^S and μ.

*Present address: Department of Electronics and Information Science, Kyoto Institute of Technology, Matsugasaki, Kyoto 606-08585, Japan.

[1] N. H. Bonadeo, J. Erland, D. Gammon, D. Park, D. S. Katzer, and D. G. Steel, Science **282**, 1473 (1998).
[2] S. Lloyd, Science **261**, 1569 (1993); A. Barenco, D. Deutsch, A. Ekert, and R. Jozsa, Phys. Rev. Lett. **74**, 4083 (1995).
[3] H. F. Hess, E. Betzig, T. D. Harris, L. N. Pfeiffer, and K. W. West, Science **264**, 1740 (1994).
[4] K. Brunner, G. Abstreiter, G. Böhm, G. Tränkle, and G. Weimann, Phys. Rev. Lett. **73**, 1138 (1994).
[5] D. Gammon, E. S. Snow, B. V. Shanabrook, D. S. Katzer, and D. Park, Science **273**, 87 (1996); Phys. Rev. Lett. **76**, 3005 (1996).
[6] M. Bayer, A. Kuther, A. Forchel, A. Gorbunov, V. B. Timofeev, F. Schäfer, J. P. Reithmaier, T. L. Reinecke, and S. N. Walck, Phys. Rev. Lett. **82**, 1748 (1999).
[7] V. D. Kulakovskii, G. Bacher, R. Weigand, T. Kümmell, A. Forchel, E. Borovitskaya, K. Leonardi, and D. Hommel, Phys. Rev. Lett. **82**, 1780 (1999).
[8] M. Bayer, O. Stern, A. Kuther, and A. Forchel, Phys. Rev. B **61**, 7273 (2000).
[9] L. Besombes, K. Kheng, and D. Martrou, Phys. Rev. Lett. **85**, 425 (2000).
[10] S. V. Gupalov, E. L. Ivchenko, and A. V. Kavokin, JETP Lett. **86**, 388 (1998); E. L. Ivchenko, Phys. Status Solidi A **164**, 487 (1997).
[11] T. Takagahara, Phys. Rev. B **60**, 2638 (1999).
[12] N. H. Bonadeo, G. Chen, D. Gammon, D. Park, D. S. Katzer, and D. G. Steel, Technical Digest of Quantum Electronics and Laser Science Conference (QELS'99, Baltimore, 1999), QTuC5, p. 48.
[13] H. Gotoh, H. Ando, H. Kamada, A. Chavez-Pirson, and J. Temmyo, Appl. Phys. Lett. **72**, 1341 (1998).
[14] T. Takagahara, J. Lumin. **87-89**, 308 (2000).
[15] J. M. Luttinger, Phys. Rev. **102**, 1030 (1956).
[16] M. G. Burt, J. Phys.: Condens. Matter **11**, R53 (1999), and references therein.
[17] T. Takagahara, Phys. Rev. B **47**, 4569 (1993).
[18] M. Sugisaki, H. W. Ren, S. V. Nair, K. Nishi, S. Sugou, T. Okuno, and Y. Masumoto, Phys. Rev. B **59**, R5300 (1999).
[19] M. Z. Maialle, E. A. de Andrada e Silva, and L. J. Sham, Phys. Rev. B **47**, 15 776 (1993).
[20] *Physics of Group IV Elements and III-V Compounds*, Vol. 17a of *Landolt-Börnstein*, edited by O. Madelung, M. Schulz, and H. Weiss (Springer, Berlin, 1982).
[21] T. Takagahara, Phys. Rev. Lett. **71**, 3577 (1993); J. Lumin. **70**, 129 (1996), and references therein.
[22] H. Kamada, H. Gotoh, H. Ando, J. Temmyo, and T. Tamamura, Phys. Rev. B **60**, 5791 (1999).